Aerodynamics of Finned Missiles at High Angle of Attack

WILLIAM L. OBERKAMPF*
The University of Texas at Austin, Austin, Texas
AND
JOHN D. NICOLAIDES†
The University of Notre Dame, Notre Dame, Ind.

A theoretical and experimental investigation of the aerodynamics of finned missiles at high angle-of-attack is presented. The interaction of the body vortex wake region with the missile fins and the resulting effect on the forces and moments produced by the fins is studied. An aerodynamic flow model is derived for a circular cylinder body at high angle-of-attack in subsonic or supersonic flow. The forces and moments produced by the fins in subsonic flow are calculated by utilizing the present flow model and present lifting theory. The experimental investigation consists primarily of strain gage measurements on a finned body in subsonic flow. The present aerodynamic flow model is compared with experimental crossflow data and good agreement between theory and experiment is obtained. Extensive comparison is made between the present force and moment predictions and available experimental data. Generally good agreement is obtained between theory and experiment for all of the forces and moments. Results given particular attention are nonlinear rolling phenomena, induced side force, and fin Magnus.

Nomenclature

a = body radius
b = fin span
C_l = roll moment coefficient ($\ell/q_\infty S_b d$)
$C_{l_i}(\alpha_b)$ = maximum amplitude of the induced roll moment coefficient for $0° < \varphi < 45°$
$C_{\bar{n}}$ = yaw moment coefficient ($\bar{n}/q_\infty S_b d$)
C_n = local normal force coefficient of fin
C_N = local normal force coefficient of fin due to angle of attack
C_y = yaw force coefficient ($F_y/q_\infty S_b$)
$C_{y_i}(\alpha_b)$ = maximum amplitude of the induced side force coefficient for $0° < \varphi < 45°$
C_z = normal force coefficient ($F_z/q_\infty S_b$)
d = body diameter
F_x,F_y,F_z = forces in the x, y, z directions, respectively (Fig. 1)
$\ell,\bar{m},\bar{n}$ = roll moment, pitch moment, yaw moment, respectively (Fig. 1)
N = normal force
N_v = total number of vortices in flow model
p = dimensionless rolling speed, $[\dot{\varphi}b/(2U_\infty)]$
p_{ss} = dimensionless steady-state rolling speed
q = dynamic pressure ($\rho U^2/2$)
r_c = radius of vortex core
$RL[\ ]$ = real part of argument
R_L = Reynolds number based on missile length, ($\rho U_\infty L/\mu$)
s = complex position in the crossflow plane ($y + iz$)
S_b = frontal area of the missile body (πa^2)
u,v,w = velocities in the x, y, z directions, respectively (Fig. 1)
U = magnitude of velocity
U_c = freestream crossflow velocity, $U_\infty \sin\alpha_b$
v_r,v_φ = velocities in the r,φ directions, respectively (Fig. 2)
$\mathbf{V}$ = velocity ($u\mathbf{i} + v\mathbf{j} + w\mathbf{k}$)
W = complex potential ($\Phi + i\Psi$)
α = angle of attack
Γ = vortex circulation, $\oint \mathbf{V}\cdot d\mathbf{s}$
δ = fin cant angle
ρ = fluid mass density
φ = roll angle
φ_{ss} = roll angle of vortex sheet separation
Φ = velocity potential
Ψ = stream function

Superscript

$(\dot{\ })$ = derivative with respect to time

Subscripts

$(\ )_b$ = missile body
$(\ )_c$ = crossflow
$(\ )_v$ = concentrated vortex
$(\ )_\infty$ = freestream conditions

Presented as paper 71-50 at the AIAA 9th Aerospace Sciences Meeting, New York, January 25-27, 1971; submitted February 5, 1971; revision received August 10, 1971. This work is based on a dissertation submitted in partial fulfillment of the requirements for the Ph.D. degree at the University of Notre Dame.

Index categories: Rocket Vehicle Aerodynamics; Uncontrolled Rocket and Missile Dynamics.

* Assistant Professor, Department of Mechanical Engineering. Associate Member AIAA.

† Professor, Department of Aerospace and Mechanical Engineering. Associate Fellow AIAA.

Introduction

A DETAILED understanding of the aerodynamics of finned missiles at high angle-of-attack has become increasingly important due to more stringent design requirements. High maneuverability and high launch angle-of-attack are two pertinent examples of recent design objectives. One of the most important characteristics of the missile flowfield at high angle-of-attack is the existence of body vortices on the lee side of the missile. This vortex wake region is not only important because of its effect on the body aerodynamics, but also because of the strong interference effects on any attached lifting surfaces.

The theoretical treatment of the body vortex wake has generally followed two different approaches; slender body theory, and an approach which will be referred to as a quasi-potential flow theory. The slender body theory approach (Refs. 1–3) is primarily concerned with the prediction of the vortex lift on bodies, whereas quasi-potential theory (Refs. 4–6) is concerned with the body vortex effects on the forces and moments produced by the fins. The present paper is an extension of the previous work in quasi-potential theory.

In the present paper a theoretical and experimental investigation of the aerodynamics of finned missiles at high angle-of-attack is presented. Of primary concern is the

effect of the body vortices at high angle-of-attack on the aerodynamic forces and moments produced by the missile fins. An aerodynamic flow model is derived for a circular cylinder body at high angle-of-attack in subsonic or supersonic flow. The viscous core region of the concentrated vortices and the vortex feeding sheets are included in the flow model. Using the velocity field calculated from the flow model and a semiempirical lifting theory, the forces and moments produced by cruciform fins in subsonic flow is calculated.

Theoretical Investigation

Previous Investigations

It was initially suggested by Lagerstrom and Graham[7] to assume that the effects of the vortex sheets were negligible and that the flow in the crossflow plane could be considered as the steady two-dimensional, potential flow about a circular cylinder with two symmetrical vortices of equal strength but opposite sign on the lee side, together with two image vortices placed within the body (Figs. 1 and 2). If the freestream flow is supersonic the additional assumption is made that the flow in the crossflow plane can be considered as incompressible. The complete three-dimensional flowfield is formed by vectorially adding the flow velocities in the crossflow plane to the axial component of velocity so that a "hybrid" flowfield is constructed.

In the crossflow plane the complex potential W is[4]

$$W = -iU_c(s - a^2/s) - i(\Gamma/2\pi)\ln[(s - s_1)(s - s_3)/(s - s_2)(s - s_4)] \quad (1)$$

where U_c is the crossflow freestream speed, i.e., $U_\infty \sin\alpha_b$, $s = y + iz$ is the position of a point in the cross-flow plane, a is the body radius, $|\Gamma|$ is the magnitude of the strength of each vortex, and $s_j = y_j + iz_4$ is the complex position of the jth vortex. The first term of Eq. (1) is the complex potential for flow about a circular cylinder at the origin and the second term is the complex potential for four vortices. The external vortices, at s_1 and s_4, are of equal strength but opposite rotational sense and they are symmetric with respect to the z axis. The image vortices, at s_2 and s_3, are also of equal strength but opposite rotational sense and are located inside the body such that the boundary condition of tangential flow at the body surface is met. Therefore, the relationships for y_j, z_j in terms of y_1, z_1 are[4]

$$y_2 = -y_3 = a^2y_1/(y_1^2 + z_1^2) \qquad y_4 = -y_1 \quad (2a)$$

$$z_2 = z_3 = a^2z_1/(y_1^2 + z_1^2) \qquad z_4 = z_1 \quad (2b)$$

With Eqs. (2a) and (2b) the only experimental quantities that must be measured in order to use the flow model are y_1, z_1, and Γ as a function of angle of attack of the body α_b and axial location on the body x (Refs. 4, 5, and 8).

The crossflow velocity components v_c and w_c can be found from

$$v_c = \partial\Phi/\partial y = RL(\partial W/\partial y) \quad (3a)$$

$$w_c = \partial\Phi/\partial z = RL(\partial W/\partial z) \quad (3b)$$

where $RL[\ ]$ symbolizes the real part of the argument.

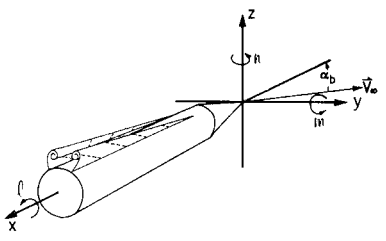

Fig. 1 Coordinate system.

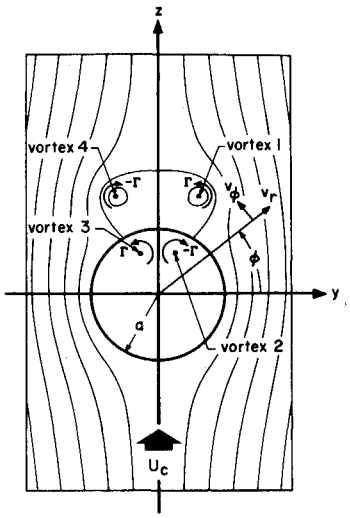

Fig. 2 Crossflow plane.

Using Eqs. (1) and (3) the crossflow velocity components become[4]

$$v_c = \frac{-2U_ca^2yz}{(y^2 + z^2)^2} + \frac{\Gamma}{2\pi}\sum_{j=1}^{4}(-1)^j\frac{z - z_j}{(y - y_j)^2 + (z - z_j)^2} \quad (4a)$$

$$w_c = U_\infty[1 + a^2(y^2 - z^2)/(y^2 + z^2)^2] - \frac{\Gamma}{2\pi}\sum_{j=1}^{4}(-1)^j\frac{y - y_j}{(y - y_j)^2 + (z - z_j)^2} \quad (4b)$$

An induced axial velocity component also exists because y_1,z_1 and Γ are functions of x. But it has been found[5] that the induced axial component is very small relative to the basic axial component $U_\infty \cos\alpha_b$ for the greater part of the flowfield. Therefore, neglecting the induced axial component, the total three-dimensional velocity field becomes

$$V = U_\infty \cos\alpha_b\mathbf{i} + v_c\mathbf{j} + w_c\mathbf{k} \quad (5)$$

Close agreement between Eq. (5) and experiment cannot be expected near the vortex centers because viscosity has been neglected. In an attempt to account for this, Jorgensen and Perkins[4] suggested that viscous vortices be superimposed onto the external and image vortices of the potential flow. Upon comparison of this suggestion with experiment it is found that poor agreement still exists.

Mello[5] suggested that the core region of the external vortices rotated as a solid body and that the velocity contributions due to the other vortices and the flow about the cylinder were zero inside the cores. Although the crossflow model of Mello did improve the agreement with experimental data, it introduced a velocity discontinuity along the edge of the vortex core because of the improper matching of the viscous and potential flows.

Present Investigation

The present investigation proposes a crossflow model similar to those previously discussed, but differs in two important aspects: first, the present model improves the approximation of the vortex core region, and second, the vortex sheets are included in the present theory. A modification of the suggestion of Jorgensen and Perkins[4] concerning the superposition of viscous vortices onto potential vortices is used in the present flow model. For the present flow model it is postulated that the viscous dissipation of each viscous vortex affects all of the contributors to the crossflow velocity in the same manner. That is, the exponential type dissipation function of each viscous vortex will now be a multiplying factor of all of the crossflow velocity terms.[9]

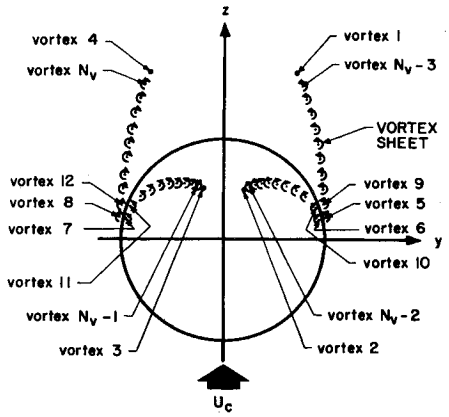

Fig. 3 Present theory for vortex sheets.

The exact location and structure of the vortex feeding sheets has not been experimentally determined as yet and consequently most of the vortex sheet details must be approximated. The vortex sheet in the present flow model will be mathematically modeled by a number of low strength discrete vortices distributed along the sheet, together with their respective image vortices inside the body (Fig. 3). It is assumed that the distribution of vorticity along the sheet is constant, so that the sheet vortices will be of equal strength and equally spaced along the sheet. With these and the previous assumptions, the crossflow velocity components become

$$v_c = \left[\frac{-2U_c a^2 yz}{(y^2+z^2)^2} + \frac{\Gamma_c}{2\pi}\sum_{j=1}^{4}(-1)^j \frac{z-z_j}{(y-y_j)^2+(z-z_j)^2} + \frac{2\Gamma_s}{\pi(N_v-4)}\sum_{j=5}^{N_v}(-1)^j \frac{z-z_j}{(y-y_j)^2+(z-z_j)^2}\right][1-e^{-C}] \quad (6a)$$

$$w_c = \left\{U_c\left[1+\frac{a^2(y^2-z^2)}{(y^2+z^2)^2}\right] - \frac{\Gamma_c}{2\pi}\sum_{j=1}^{4}(-1)^j \times \frac{y-y_j}{(y-y_j)^2+(z-z_j)^2} - \frac{2\Gamma_s}{\pi(N_v-4)}\sum_{j=5}^{N_v}(-1)^j \times \frac{y-y_j}{(y-y_j)^2+(z-z_j)^2}\right\}\{1-e^{-C}\} \quad (6b)$$

where

$$C = 1.254[(y-y_v)^2+(z-z_v)^2]/r_c^2 \quad (6c)$$

and

$$y_v, z_v = \begin{cases} y_1, z_1 & y \geq 0 \\ y_4, z_4 & y < 0 \end{cases}$$

and N_v is the total number of vortices, Γ_c is the strength of the concentrated vortex, Γ_s is the total vortex strength of each sheet (excluding the concentrated vortex), and r_c is the vortex core radius. The dependence of $\Gamma_c, \Gamma_s, y_1, z_1$, and r_c on angle of attack and body length are taken from experimental results of Mello[5] and Fiechter.[8]

The relations between s_5, s_6, s_7, etc. are analogous to the relations between s_1, s_2, s_3, and s_4 as given by Eqs. (2), so that in general one has for $j = 2,6,10, \ldots N_v - 2$

$$y_j = -y_{j+1} = a^2 y_{j-1}/(y_{j-1}^2 + z_{j-1}^2)$$
$$z_j = z_{j+1} = a^2 z_{j-1}/(y_{j-1}^2 + z_{j-1}^2) \quad (6d)$$

for $j = 4,8,12 \ldots N_v$

$$y_j = -y_{j-3} \text{ and } z_j = z_{j-3}$$

With Eqs. (6d) the location of all the vortices can be related to the location of the vortices external to the body in the positive y-z quadrant, i.e., s_1, s_5, s_9, etc. (Fig. 3).

The approximate location of the vortex sheets is empirically determined from the experimental data of Mello.[5] From his experimental contours of local total pressure in the crossflow plane an expression was found for the approximate location of the right-hand vortex sheet. The following expression gives a reasonable estimation of the sheet location as a function of roll angle, angle-of-attack, and body length

$$s_s = [a\cos(\pi\varphi/2\varphi_1) + r_1 \sin^2(\pi\varphi/2\varphi_1)/\{1 + r_1(\varphi_1 - \varphi)/a\}]e^{i\varphi} \quad \varphi_{ss} \leq \varphi \leq \varphi_1 \quad (7a)$$

where r_1, φ_1 is the radial and angular location, respectively, of vortex 1, and φ_{ss} is the angle at which the sheet separates from the body. φ_{ss} is defined by the equation

$$\cos(\pi\varphi_{ss}/2\varphi_1) + (r_1/a)\sin^2(\pi\varphi_{ss}/2\varphi_1)/[1 + r_1(\varphi_1 - \varphi_{ss})/a] = 1.01 \quad (7b)$$

As stated earlier, the low strength vortices which represent the vortex sheet are equally spaced in arc length along the sheet. The arc length of the vortex sheet is

$$L_s = \int_{\varphi_{ss}}^{\varphi_1}\left[r_s^2 + \left(\frac{dr_s}{d\varphi}\right)^2\right]^{1/2} d\varphi \quad (8)$$

where r_s is the magnitude of s_s. The first vortex in the sheet, vortex number 5, is located at the point where the sheet leaves the body so that $r_5 = 1.01a$ and $\varphi_5 = \varphi_{ss}$. The angular position $\varphi_j, j = 5,9,13 \ldots N_{v-3}$ of a vortex in the sheet is found from

$$\left(\frac{j-5}{N_v-4}\right)L_s = \int_{\varphi_{ss}}^{\varphi_j}\left[r_s^2 + \left(\frac{dr_s}{d\varphi}\right)^2\right]^{1/2} d\varphi \quad (9a)$$

Once the angular position is known from Eq. (9a), then from Eq. (7a) one obtains the radial location.

$$r_j = a\cos(\pi\varphi_j/2\varphi_1) + r_1\sin^2(\pi\varphi_j/2\varphi_1)/[1 + r_1(\varphi_1 - \varphi_j)/a] \quad (9b)$$

where $j = 5,9,13, \ldots, N_v - 3$.

With Eqs. (7, 8, and 9), the location of sheet vortices numbers $5,9,13, \ldots, N_v - 3$ is known and, therefore, can be used with Eqs. (6d) to find the position of all the vortices in the flow model. In the present investigation the number of vortices in each sheet was set at 10, so that the total number of vortices in the flowfield was 44. With the position and strength of all the vortices known, Eqs. (6a) and (6b) are used to calculate the total crossflow velocity at any point in the flow field. All of the calculations for the present flow model were performed on a UNIVAC 1107 digital computer.

Prediction of Fin Forces and Moments

The forces and moments produced by cruciform fins in incompressible flow are calculated by using the flow model in conjunction with the present lifting theory. The lifting theory is basically a strip theory, i.e., it is assumed that the fin can be divided up into differential elements, each of which are independent. The total force is then calculated by integrating over the surface of the fin. The local normal force on a differential element of the fin surface is written as

$$dN = C_n q dx dr \quad (10)$$

where C_n is the local normal force coefficient and q is the local dynamic pressure. The local normal force coefficient C_n will be composed of the product of three separate functions: first, the normal force due to the local angle-of-attack of the differential element; second, the local chordwise distribution; and third, the local spanwise distribution.

The chordwise and spanwise distribution functions were chosen so that the normal force distribution for uniform

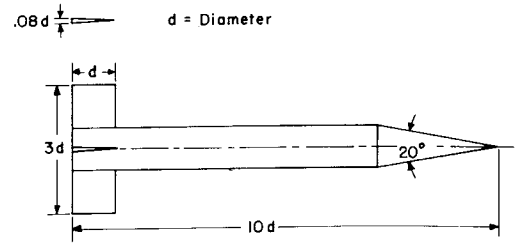

Fig. 4 Basic finner missile.

approach flow would agree qualitatively with experimental data (See Ref. 9). The local normal force coefficient C_n is written as

$$C_n = \eta C_N(b_o - a)(1 + 4\xi^3/3)(1 - \xi^2)^{1/2}(x_{te} - x)^2/a^3 \quad (11)$$

where $\xi = (r - a)/(b_o - a)$, η is a constant, b_o is the semi-span of the fin, x_{te} is the x coordinate of the trailing edge of the fin, and C_N is the local normal force coefficient of the fin due to local angle-of-attack. The constant η is a dimensionless scale factor which can be evaluated by the requirement that the integrated average of the assumed distribution over the fin surface be unity. The functional dependence of C_N on α was experimentally measured for the condition of uniform approach flow to a square planform fin (Ref. 9). With the empirical relationship between C_N and α, C_N in Eq. (11) is found by calculating the local angle-of-attack of the differential fin element. The local angle-of-attack is defined to be the angle between the local velocity and the chord line of the fin. The local velocity is known from the present flow model and the orientation of the chord line can be found as a function of roll angle of the fin and fin cant.

The local normal force coefficient, Eq. (11), is now substituted into Eq. (10) so that the differential normal force is known for each element of the fin surface. To calculate the total force due to the fins, Eq. (10) is integrated over the four fin surfaces. To calculate the fin produced moments, the appropriate moment arm is multiplied by Eq. (10) and then integrated.

Experimental Investigation

The experimental investigation consisted of four programs: first, strain gage measurements of the induced roll moment and fin cant moment on the basic finner missile; second, qualitative dynamic roll lock-in measurements on the basic finner missile; third, strain gage measurements of the normal force and pitch moment on a body of revolution and finned missile; fourth, strain gage measurements of the yaw force and moment on a finned missile. All of the experimental programs were conducted in subsonic wind tunnels at the Department of Aerospace and Mechanical Engineering, University of Notre Dame.

The induced roll moment was measured on the basic finner missile (Fig. 4) for zero fin cant and through the angle-of-attack range, 0° to 25°, and at four Reynolds numbers (based on body length); 0.45×10^6, 0.69×10^6, 0.92×10^6, and 0.90×10^6 with a boundary-layer trip. The fin cant moment was measured at zero angle of attack and through the fin cant range of 0° to 7° and at three Reynolds numbers; 0.43×10^6, 0.67×10^6, and 0.90×10^6. The fin cant moment and the induced roll moment were also measured in combination for 4° of fin cant and through the angle-of-attack range 0° to 20°, and at two Reynolds numbers; 0.69×10^6 and 0.92×10^6.

Dynamic roll lock-in tests were conducted in order to confirm qualitatively the strain gage data. Roll lock-in can only occur if the roll moment is zero and the derivative of the roll moment with respect to roll angle is negative, i.e., $\partial l/\partial\varphi < 0$, at a particular roll angle. By simply observing the roll motion it can be concluded if roll lock-in occurred. Dynamic roll lock-in data were taken for zero fin cant and through the angle-of-attack range of 5° to 20° and at four Reynolds numbers based on body length: 0.45×10^6, 0.69×10^6, 0.92×10^6, and 0.90×10^6 with a boundary-layer trip.

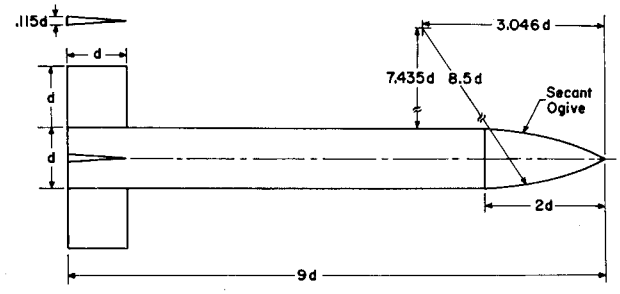

Fig. 5 Finned missile used for normal force and yaw force measurements.

The normal force and pitch moment and yaw force and moment were measured on a finned body, shown in Fig. 5. The finned body was similar to the basic finner; however, the finned body had a secant ogive nose and was 9 diam long. The force and moment measurements were made by use of semiconductor strain gages and for the conditions of zero fin cant, angle-of-attack range of 0° through 25°, and at a Reynold's number (based on body length) of 1.11×10^6.‡

Discussion of Results

Aerodynamic Flow Model

The present aerodynamic flow model will be briefly evaluated by comparing theoretical and experimental crossflow velocity components. Figure 6 shows the theory and experiment for the radial crossflow velocity v_r and the tangential crossflow v_φ for $M_\infty = 2.$, $\alpha_b = 20°$, $x/d = 6.57$ and $\varphi = 45°$. Fair agreement is indicated between the theory and experiment in Fig. 6a. Figure 6b presents good agreement

a) v_r/U_∞ vs r/a

b) v_ϕ/U_∞ vs r/a

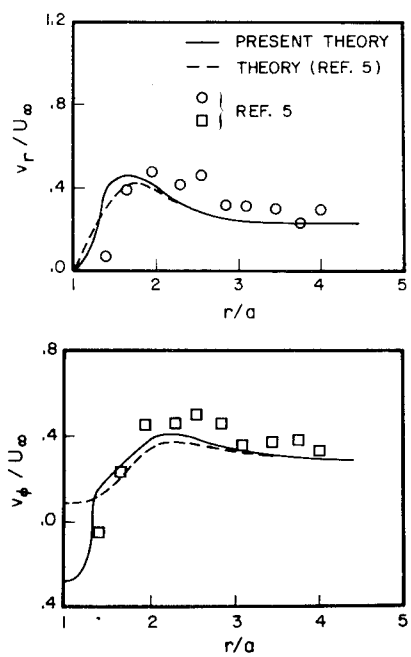

Fig. 6 Crossflow velocity components for $M_\infty = 2$, $\alpha_b = 20°$, $x/d = 6.57$ and $\phi = 45°$.

‡ Only a small portion of the experimental data is presented here. For a complete documentation, see Ref. 9.

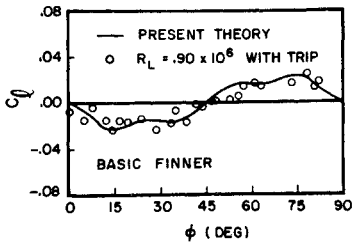

Fig. 7 Induced roll moment coefficient vs roll angle for $\alpha_b = 10°$.

between the theory and experiment, especially near the body surface. It is observed that near the surface v_φ is negative. This indicates that the flow has separated from the body and a reverse flow region has formed. For the conditions stated in the figure, the vortex sheet is located just off the surface and, therefore, the velocity components of the sheet vortices tend to hasten flow separation.

The good agreement between the theory and the experimental data near the surface, even though the rate of change of v_φ with r is very large, indicates that the approximation for the location of the vortex sheet was reasonably accurate.

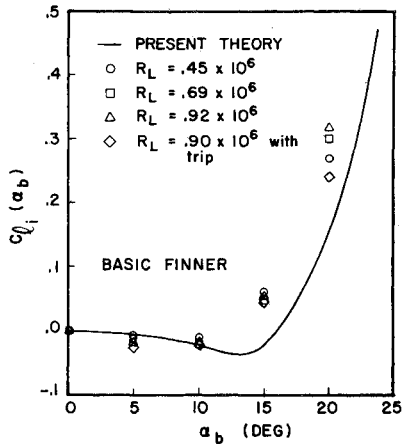

Fig. 8 Amplitude of the induced roll moment coefficient vs angle-of-attack.

It is noted in Fig. 6b that near the body surface v_φ as predicted by the present theory is considerably different from that predicted by Mello. The difference between the two theories is due to the vortex sheets in the present flow model. The vortex sheets in combination with the concentrated vortices produce a much stronger separation mechanism than concentrated vortices alone.

Roll Moments

All of the theoretical and experimental roll moment data apply to the basic finner missile in low subsonic flow. Figure 7 presents the theoretical and experimental induced roll moment coefficient vs roll angle for $\alpha_b = 10°$. It is seen that good agreement is obtained between theory and experiment. For this angle of attack $C_{l_i}(\alpha_b)$ is negative, where $C_{l_i}(\alpha_b)$ is defined as the maximum amplitude of the induced roll moment coefficient for any value of roll angle between 0° and 45°.

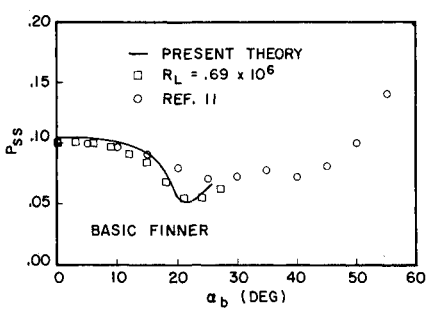

Fig. 9 Steady state rolling speed vs angle-of-attack for $\delta = 4°$.

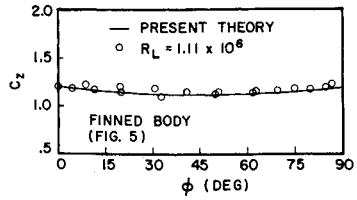

Fig. 10 Normal force coefficient due to fins vs roll angle for $\alpha_b = 7°$.

Figure 8 shows the experimental and theoretical amplitude of the induced roll moment coefficient, $C_{l_i}(\alpha_b)$, vs angle-of-attack for the four Reynolds numbers tested. It is observed from this figure that the present theory yields good agreement for intermediate angle of attack, but for large α_b, the theory is appreciably low. Although the theory predicts an extremely rapid increase in $C_{l_i}(\alpha_b)$ for large α_b, the experimental data increases even more rapidly. It was found from computer experiments with the present theory that the two primary aerodynamic characteristics which were responsible for the strong nonlinear nature of $C_{l_i}(\alpha_b)$ were the vortex core region and stall of the fin.

Now consider the theory and experiment for the steady state rollspeed vs angle-of-attack for 4° of fin cant (Fig. 9). It is observed from Fig. 9 that the theory and experiment are in good agreement for angle-of-attack up to 25°. The range $10° < \alpha_b < 20°$ is usually called the roll slow-down region and has been measured on several other finned missile configurations (Ref. 10). The region of sharp increase in p_{ss} for very large angle-of-attack is called the roll speed-up region. The present theory cannot be applied to the roll speed-up region because at these very large angles of attack the wake region becomes asymmetrical (Refs. 4 and 8).

Normal Force

To obtain an accurate evaluation of the present theory for the normal force due to the fins, the contribution of the body of revolution to the normal force must be precisely known. Therefore, as part of the experimental program, the normal force of the nonfinned missile was measured at the same angle-of-attack and Reynolds number as the tests on the finned body shown in Fig. 5. The experimental data of the body of revolution was then subtracted from the finned body data so that the contribution of the fins could be obtained. Simply subtracting the data of the body of revolution from that of the finned body to find the fin contribution is a valid technique if the assumption is made that the effect of the fins on the body flowfield is small. This assumption is fulfilled in the present case because first, the ratio of the root chord of the fin to the body length is small, and second, the fin-body juncture is adjacent to the base of the body.

Shown in Fig. 10 is the theory and experiment for the normal force coefficient due to the fins, C_z, vs roll angle for an angle of attack of 7°. Very good agreement is noted in Fig. 10 between the theory and experiment. It is also observed in this figure that the normal force is slightly smaller at $\varphi = 45°$ as compared to $\varphi = 0°$.

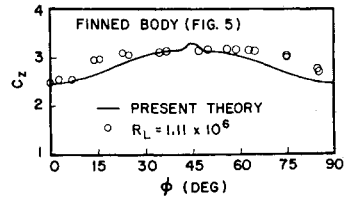

Fig. 11 Normal force coefficient due to fins vs roll angle for $\alpha_b = 20°$.

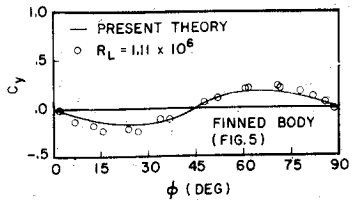

Fig. 12 Side force coefficient vs roll angle for $\alpha_b = 15°$.

The theory and experiment for the normal coefficient due to fins vs roll angle for $\alpha_b = 20°$ is shown in Fig. 11. Very good comparison is obtained between the theory and experiment over the entire range of roll angle. It is observed from Fig. 11 that the variation of C_z with φ has changed considerably from $\alpha_b = 7°$. Normal force vs roll angle now has the characteristic that C_z at $\varphi = 45°$ is approximately 30% higher than C_z at $\varphi = 0°$. From computer experiments with the theory it was found that this characteristic is explained by first noting that for $\alpha_b = 20°$, the fin at $\varphi = 0°$ (or 180°) is entirely in the poststall angle-of-attack range. When the roll angle increases, the local α decreases all along the span so that the local normal force decreases. But then portions of the fin attain the stall angle, i.e., the angle-of-attack of maximum normal force. Here the local normal force increases sharply and thereby causes the total normal force coefficient due to the fins to increase.

Yaw Force and Moment

The yaw force and moment produced by the fins will be divided into two general types; first, side force§ and moment, which is defined only for the roll angle constant with time, and second, fin Magnus force and moment, which is defined only for relatively large roll rates. The latter of the two forces and moments is referred to as Magnus in the broad sense because a Magnus force or moment may be considered as any force or moment that is generated by a spinning vehicle with crossflow.

The distinction between side force and moment and Magnus force and moment may be admittedly vague at times in actual missile flight cases. The distinction, however, is made because in the present theory they are calculated by different procedures. The side force and moment are calculated from the theory by simply setting $\dot{\varphi} = 0$. The fin Magnus force and moment is calculated by averaging the yaw force and moment through a roll cycle for $\dot{\varphi} > 0$.

Shown in Fig. 12 is the theory and experiment for the induced side force coefficient vs roll angle for $\alpha_b = 15°$. Very good agreement is demonstrated in this figure between theory

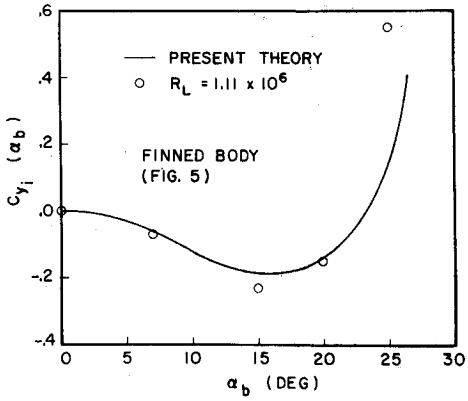

Fig. 13 Amplitude of the induced side force coefficient vs angle-of-attack.

§ This force is sometimes called the induced side force because it is "induced" by body-fin interference.

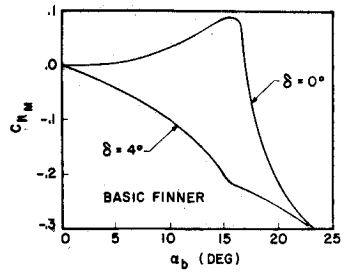

Fig. 14 Present theory for fin Magnus moment coefficient vs angle-of-attack for $p = 0.10$.

and experiment. It is observed that $C_{y_i}(\alpha_b)$, i.e., the maximum amplitude of the induced side force coefficient for $0° < \varphi < 45°$, is negative. It is also noted from the figure that for purposes of missile flight dynamics, the induced side force coefficient could be analytically approximated by a circular sine function of the form $C(\alpha_b) \sin 4\varphi$. For angles-of-attack higher than 15°, it was found from both theory and experiment that the approximation should be of the form $C_1(\alpha_b) \sin 4\varphi + C_2(\alpha_b) \sin 8\varphi$.

Figure 13 shows the theoretical and experimental maximum amplitude of the induced side force coefficient $C_{y_i}(\alpha_b)$ vs angle-of-attack. For angle-of-attack less than about 22°, the theory is in very good agreement with the experimental data, but for $\alpha_b > 22°$, the theory is substantially low. It is also noted that the trend of $C_{y_i}(\alpha_b)$ is remarkably similar to that of $C_{l_i}(\alpha_b)$ vs α_b. It was found from the theory that the extremely rapid increase in $C_{y_i}(\alpha_b)$ with α_b is also due to the body vortex cores and fin stall.

Now consider the theoretical predictions for fin Magnus. The two primary variables of Magnus are usually roll rate and angle-of-attack. When fin Magnus is considered, however, another variable must be added, fin cant. The first investigator to suggest the existence of a Magnus moment due to fin cant was Bolz.[12] Fin cant Magnus was later analyzed for supersonic flow by a simple approach due to Benton.[13] Although the moment calculated by Benton is generically the same as the present fin cant Magnus moment, there is a substantial difference between the two. Benton assumed that there is no interference between the body and the fins and also that the missile is at a roll orientation angle of 0°.

The theoretical prediction for fin Magnus moment coefficient, C_{n_M}, vs angle-of-attack for $p = 0.10$ and $\delta = 0°$ and 4° is shown in Fig. 14. It is seen from this figure that the fin cant greatly changes the character of the Magnus moment. For $\delta = 0°$, Magnus is highly nonlinear with angle-of-attack. For $\delta = 0°$ and $\alpha_b < 17°$, fin Magnus is roughly proportional to α_b^3, but for $\alpha_b > 17°$ the Magnus moment sharply drops to zero and becomes large negatively. For $\delta = 4°$, the theory predicts that the fin cant Magnus will cause the total fin Magnus moment to be negative for the angle-of-attack range considered.

Conclusions

A theoretical and experimental investigation of the aerodynamics of finned missiles at high angle-of-attack is presented. Of primary concern is the interaction of the body vortex wake with the missile fins and the resulting effect on the forces and moments produced by the fins. From the generally good agreement between theory and experiment it is believed that the validity of the present approach is proven. The present theory should prove useful not only for explaining certain flight dynamic instabilities, but also for successful missile designs in the future.

References

[1] Mangler, K. W. and Smith, J. H. B., "A Theory of the Flow Past a Slender Delta Wing with Leading Edge Separation," *Proceeding of the Royal Society*, Ser. A, Vol. 251, 1959, pp. 200–217.

[2] Smith, J. H. B., "Improved Calculations of Leading-Edge Separation from Slender Delta Wings," TR 66070, March 1966, Royal Aircraft Establishment, London.

[3] Levinsky, E. S. and Wei, M. H. Y., "Nonlinear Lift and Pressure Distribution of Slender Conical Bodies with Strakes at Low Speeds," CR-1202, Oct. 1968, NASA.

[4] Jorgensen, L. H. and Perkins, E. W., "Investigation of Some Wake Vortex Characteristics of an Inclined Ogive-Cylinder Body at Mach No. 2," Rept. 1371, May 1955, NACA.

[5] Mello, J. F., "Investigation of Normal Force Distributions and Wake Vortex Characteristics of Bodies of Revolution at Supersonic Speeds," *Journal of the Aeronautical Sciences*, Vol. 26, No. 3, March 1959, pp. 155–168.

[6] Mello, J. F. and Sivier, K. R., "Supersonic Induced Rolling-Moment Characteristics of Cruciform Wing Body Configuration at High Angles of Attack," *Aerospace Engineering*, Vol. 20, No. 7, July 1961, pp. 20–21, 44–51.

[7] Lagerstrom, P. A. and Graham, M. E., "Aerodynamic Interference in Supersonic Missiles," SM 13743, July 1950, Douglas Aircraft Corp., Long Beach, Calif.

[8] Fiechter, M., "On the Vortex System of High Fineness Ratio Bodies of Revolution and Their Influence on the Aerodynamic Coefficients," Rept. 10/66, Dec. 1966, German-French Research Inst. of St. Louis, St. Louis, France.

[9] Oberkampf, W. L., "Aerodynamics of Finned Missiles at High Angle of Attack," Ph.D. dissertation, Aug. 1970, Univ. of Notre Dame, Notre Dame, Ind.

[10] Nicolaides, J. D., "Missile Flight and Astrodynamics," TN-100A, 1961, Bureau of Naval Weapons, Dept. of the Navy, Washington, D.C.

[11] Greene, J. E., "An Investigation of the Rolling Motion of Cruciform-Fin Configurations," Rept. 6262, March 1960, Naval Ordnance Lab., White Oak, Md.

[12] Bolz, R. E., "Dynamic Stability in Rolling Flight," *Journal of Aeronautical Sciences*, Vol. 19, No. 6, June 1952, pp. 395–403.

[13] Benton, E. R., "Supersonic Magnus Effect on a Finned Missile," *AIAA Journal*, Vol. 2, No. 1, Jan. 1964, pp. 153–155.